The effect of energetic particle beams on chromospheric emission of 25th July 2004 flare

The effect of energetic particle beams on the chromospheric emission of the 25th July 2004 flare

V. V. Zharkova[1][*], L. K.Kashapova[2], S.N.Chornogor[3] and O.V.Andrienko[3,4]

[1]*Department of Mathematics, University of Bradford, Bradford, UK*
[2]*Institute of Solar-Terrestrial Physics, SB RAN, Irkutsk, Russia*
[3] *Main Astronomical Observatory, NASU, Kyiv, Ukraine*
[4] *IC AMER, NASU, Kyiv, Ukraine*

ABSTRACT
In this paper a role of particle beams for generation of a close spatial and temporal correlation between hard H-ray (HXR) energy and Hα line emission bursts in the solar flare of 25 July 2004 is discussed. The light curves in HXR emission and Hα line revealed the pre-flare and main flare events correlated with the variations of a line-of-sight (LOS) magnetic flux. HXR emission shows the three main bursts during the main flare phase which are accompanied by Hα intensity increases. The latter appear in 10 locations (kernels) at different times in succession; the kernel locations are associated with strong magnetic sources situated on the opposite sides from the magnetic neutral line (MNL). The appearance of Hα kernels in the pre-flare event and those at the start of the main event are correlated very closely (within a few seconds) with the HXR emission observed by RHESSI (HXR+Hα kernels), while the appearance of some other ones, not associated with HXR emission, was delayed by ten of seconds. Electron beam parameters were derived from the RHESSI spectra in where the observed HXR photon flux was corrected for the self-induced electric field effect. Possible implications of this electric field on production of the transient magnetic fields observed during the flare are discussed. The Hα emission observed during the first burst was simulated in hydrodynamic atmospheres for 5 level plus continuum hydrogen atom with the full non-LTE approach combining radiative, thermal and non-thermal excitation and ionization by an electron beam with the derived parameters. The simulated temporal profiles of Hα emission produced by non-thermal hydrogen excitation revealed a very good fit to the observed ones in the HXR+Hα kernels and 10-20 s delays in the other kernels. This allows to speculate that Hα emission in these kernels is caused mainly by electrons in the HXR+Hα kernels and mainly by protons in the other ones.

Key words: Sun: flares; Sun: particle beams; Sun: chromosphere; Sun: non-thermal radiation

1 INTRODUCTION

There is often a close (up to 1 sec) temporal correlation in spectral observations of hard X-ray, UV and optical emission from a flare appearing from different atmospheric depths (Cheng, Orwig, and Tandberg-Hanssen 1987; Hiei 1987; Kurokawa, Takakura and Ohki 1988; Asai *et al.* 2000; Bianda *et al.* 2005). These fast temporal fluctuations in hard X-ray and optical emission can only be attributed to propagation of fast beams of accelerated particles (electrons or protons) and to dissipation of their energy in lower atmo-

spheric layers via non-thermal excitation and ionization and heating of the ambient plasma (Hudson 1972; Ricchiazzi and Canfield 1983; Henoux 1991; Zharkova & Kobylinskij 1993; Metcalf *et al.* 2003; Allred *et al.* 2005). The investigation of non-thermal hydrogen emission caused by beam electrons helped to explain a close temporal correlation between HXR and optical emission. However, it raised other questions on exact scenarios of the generation of such particles during a flare, how these spectral changes are related to the magnetic structures and what kind of interaction there is between accelerated particles and ambient neutral atoms throughout the whole atmospheric depth of a flare.

This is why many authors paid special attention to the

[*] E-mail: v.v.zharkova@brad.ac.uk (VVZ); lkk@iszf.irk.ru (LKK)

2   *V. V. Zharkova, L.K.Kashapova, S.N.Chornogor and O. V. Andrienko*

investigation of rapid variations of the Hα line intensity and its correlation with HXR flux during the impulsive phase of chromospheric flares e.g. (Trottet *et al.* 2000) and references therein. This often includes a comparison of the spatial distribution of hard X-ray sources and Hα flare kernels (Asai *et al.* 2000) showing that many Hα kernels become brightening in succession during the evolution of flare ribbons. These brightenings are assumed to follow the process of consequent energy release in the flare with a very complicated magnetic structure and to establish that some Hα kernels coincide with hard X-ray sources while the others do not.

For example, in the multi-wavelength investigation of a few solar flares by Kašparová *et al.* (2005a,b) considerable attention was paid to the locations of fast changes of Hα intensity and their association with hard X-ray (HXR) sources. The HXR sources are found to be located on the external edges of the Hα emission and often connected with the chromospheric plasma heating by non-thermal electrons as predicted by some solar flare models (Zharkova & Kobylinskij 1993; Metcalf *et al.* 2003). However, the fast changes of Hα intensity are located not only inside the hard X-ray sources, as expected, if they are the signatures of the chromospheric response to the electron bombardment, but also outside them. This fact may indicate that the response of the lower atmosphere to a flare energy release is not only restricted to the sites of propagation of accelerated electrons only, but can be associated with some other agents (Zharkova & Gordovskyy 2004; Kašparová *et al.* 2005a,b).

Furthermore, the Hα emission in the impulsive phase of solar flares, which increases simultaneously with HXR emission, was simulated by using different electron beam kinetics: electron flux conservation (Kašparová *et al.* 2005a,b) and continuity equation (Zharkova & Kobylinskij 1993). There was a significant difference revealed in the Hα line profiles: beam electrons are found to affect different parts of the profile depending on the beam kinetic model considered: the line core for the flux conservation equation or the line wings for the continuity equation. As a result, the full Hα emission, e.g. integrated in wavelengths within the line profile, are different as well, revealing that the continuity equation approach produces lower magnitudes of integrated Hα emission than the other approach. This difference needs to be addressed for the future studies.

In addition, most previous studies of correlation between the emission in chromospheric lines and HXR response were carried out only for larger solar flares while small-scale events in the chromospheric emission were usually ignored. The high-resolution RHESSI observations have a good photon sensitivity this allows to carry out the investigation of much smaller flares and even to trace a pre-flare activity in an active region that was identified in the flare 25 July 2004 of class M. This flare was also observed with high temporal and spatial resolution VTT instrument in the Taide Observatory, Tenerife that provided a set of small-scale Hα kernels appeared in succession in the two ribbon flare. These observations offer a unique opportunity to investigate the processes of energy release and transport during the moderate solar flare with a complex magnetic structure.

Therefore, in the current paper we aims to investigate multi-wavelength emission obtained for the pre-flare and main flare of the 25 July 2004 and interpret the kernels with HXR and Hα emission with the advanced models of par-
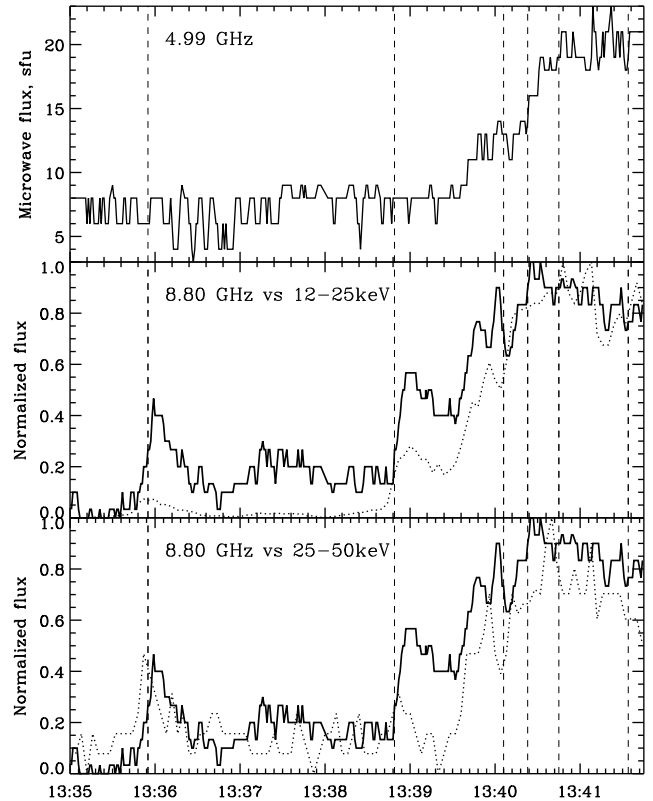

Figure 1. *Temporal evolution of microwave flux by Radio Solar Telescope Network (RSTN) and hard X-ray flux (RHESSI). Microwave flux is shown by solid line, HXR flux is dotted line. The dashed lines correspond to the event of fast rising of intensity on Hα images during the 25th July 2004 flare.*

ticle acceleration, precipitation and radiative transfer with non-thermal excitation and ionization developed in the recent years. The observations used are described in section 2, the kinetic, hydrodynamic and radiative models used to fit the Hα observations are described in section 3 and the conclusions are drawn in section 4.

2   OBSERVATIONS

The M2.2 class flare of the July 25 2004 occurred in NOAA Active Region 10652, started at 13:37 UT and ended at 13:55 UT, had maximum at 13:49 UT. Note, that the information about optical importance of the flare is absent (no patrol observations are available).

For the multi-wavelength analysis of this flare, we used the following data:

● Optical observations in the Hα line slit-jaw images from the Vacuum Tower Telescope (VTT), Observatorio del Teide, Tnefire, Spain. The cropped images covering some rectangles related to slit were taken in succession (with a 5 second cadence) in the two chromospheric lines (Hα and CaII K) and white light emission. The duration of the series was usually about 1-2 minutes. Observations lasted for the time interval 13:24:26 - 14:17:52 UT that covers both the pre-flare events and the flare itself.

The effect of energetic particle beams on the chromospheric emission 3

• Full disk magnetograms and intensitygrams provided by the SOHO Michelson Doppler Imager (MDI)Scherrer *et al.* (1995). Note: intensitygrams were used for establishing the precise heliographic coordinates for the Hα data.

• Hard x-ray data in different bands obtained by Reuven Ramaty High Energy Solar Spectroscopic Imager (RHESSI) described by (Lin *et al.* 2002). The RHESSI HXR data were analyzed with the software developed by the RHESSI team Schwartz *et al.* (2002) including the pile-up and albedo corrections (Kontar *et al.* 2006).

• Active region images in 195 Å and 1600 Å continuum by Transition Region and Coronal Explorer(TRACE) described by (Handy *et al.* 1999). We used 195 Å images by TRACE both for investigation of energy release processes at higher layers of the solar atmosphere and tuning the heliographic coordinates for Hα data.

The light curves of hard X-ray (HXR) emission of this flare observed in different bands by the RHESSI (the counts corrected for pile-up and albedo effects obtained with a 4 second time resolution) and and the microwave flux by RSTN (obtained with 1 second temporal resolution) are presented in Figure 1 clearly showing a burst-like structure. There are two events observed for the light curves: the pre-flare one occurring around 13:35:00 UT and the main event occurring after 13:37:00 UT. The spikes of HXR and radio emission were also accompanied by small-scale chromospheric events observed in Hα light curves and images discussed in sections 2.1) and 2.2.

2.1 Hα emission in the pre-flare event

The preliminary multi-wavelength study of the pre-flare event occurred on July 25, 2004 (Chornogor *et al.* 2005) from 13:34:00 UT to 13:37:00 UT is resumed in the current paper by using RHESSI, Hα, TRACE, and MDI observations obtained for AR 0652 (N08W35). The temporal variations of Hα emission in this pre-flare event have shown rather a close temporal correlation with the second and third maxima in HXR emission observed in 12–25 keV from this event (Fig. 2).

In order to detect the locations of fast Hα emission changes during the pre-flare event we carried out a subtraction of the two consequent images, namely: from all images of the series the image for the first moment obtained at 04:13:35 UT was subtracted. Then for the whole time series a further subtraction was carried out between the two images nearest in time. In order to determine the heliographic coordinate system in the region, we use for the final tuning SOHO/MDI intensitygrams and 1600 Å TRACE images. The accuracy of the heliographic coordinate determination is about 2 arcseconds.

For the analysis of the locations of Hα emission in the pre-flare event with respect to the HXR sources, we reconstructed the source images for 12–25 keV and 25–50 keV bands from 13:35:44 UT to 13:36:16 UT by using PIXON algorithm (Puetter and Pina 1994; Metcalf *et al.* 1996) and overlaid them on the Hα, 1600 Å and Hα difference image. The results are shown in Fig 3 for different times.

There are two locations where the sharp increases of Hα line intensity is observed: the location "A" occurred on the south-west from the HXR source and the location "B" oc-
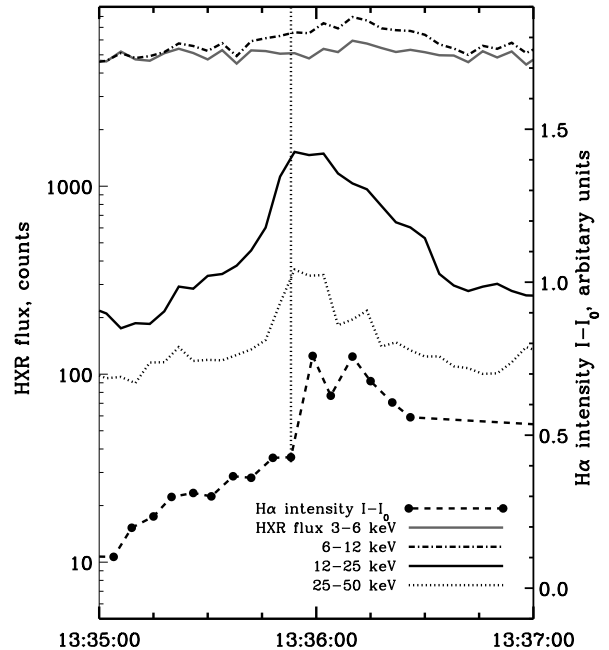

Figure 2. Temporal evolution of hard X-ray flux (RHESSI)and the Hα intensity for the kernel "B". The dotted line corresponds to the moment when the event "B" first appeared.

curred on the north from it (see Fig. 3, left and middle plots). The event "B" is seen to be located inside the 12–25 keV band source and outside the 25-50 keV band source. Later this source in the location B coincided with the locations of some Hα kernels in the main event. In addition, these two sources (A and B) are recorded in the 1600 Åemission measured by TRACE (Fig. 3, right plot).

The locations of the increased Hα line emission having such the temporal variations marked by the dotted orange line in Fig. 3 are found to occur in the core "B". However, there is no noticeable Hα emission inside the area of the HXR source of 25–50 keV while there is some brightening seen in 1600 Å emission (Fig. 3, right). Unfortunately, the moments of the fast variations of Hα emission in the source "A" were missed.

The event can be classified as the pre-flare one because it occurred in the areas spatially coincided with the future location of the main event; also the peaks of Hα emission were temporarily over-lapped with the start of the increase of 3-12 keV emission observed in the the main flare event. The similar type of a pre-flare event was described in Battaglia, Fletcher, & Benz (2009). Moreover, the further analysis shows that this event was a part of the same HXR and magnetic field changes occurred in the flare as discussed in section 2.4.

2.2 Fast changes of Hα emission in the main flare event

In the main flare event, the fast changes of Hα intensity observed by VTT before the flare maximum are also correlated rather closely with the HXR emission observed by RHESSI (Figure 4). Similarly to the pre-flare event, in order to search for fast intensity increases, the difference Hα in-

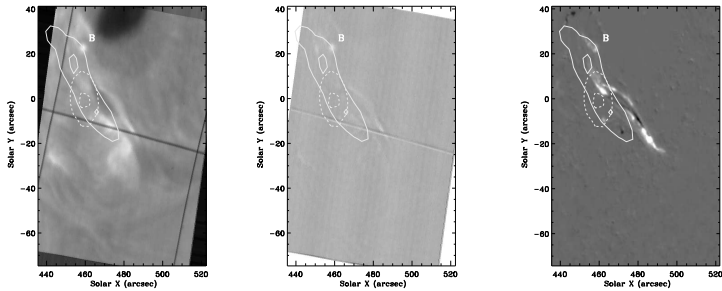4   *V. V. Zharkova, L.K.Kashapova, S.N.Chornogor and O. V. Andrienko*

Figure 3. The images of the source B (see the text for details) in the pre-flare event (from the left to right): the Hα line image at 13:35:53 UT; the difference intensity image in Hα (13:35:53-13:35:48UT); the difference intensity image in 1600 Å band (13:35:01-13:35:46 UT). The RHESSI images obtained for the interval 13:35:44 -13:36:16 UT in the bands of 12-25keV and 25-50 keV are plotted as the solid and dashed contours obtained at 50 and 90% of the image maximum, respectively.
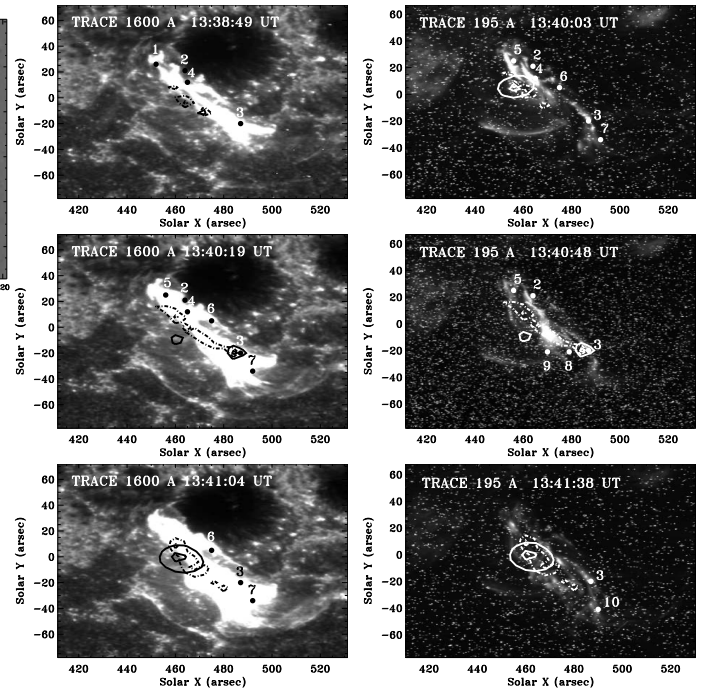

Figure 4. *Temporal evolution of hard X-ray flux (RHESSI) (the left axis Y) and the Hα intensity (the right axis Y) for different kernels which locations are shown in Figure 5. The dashed line shows the beginning of the RHESSI night time. I_0 is the initial intensity of the relevant kernels.*

Figure 5. The main flare event: evolution of Hα emission kernels and HXR sources versus the TRACE image of the same region in 195 Å and 1600 Å . Hα emission kernels are marked as the black points which number corresponds to the order of their onset. The HXR sources are plotted as the contours at the levels of 50 and 90% from their maximum. 12-25 keV and 25-50 keV bands are plotted by the dashed and solid contours, respectively.
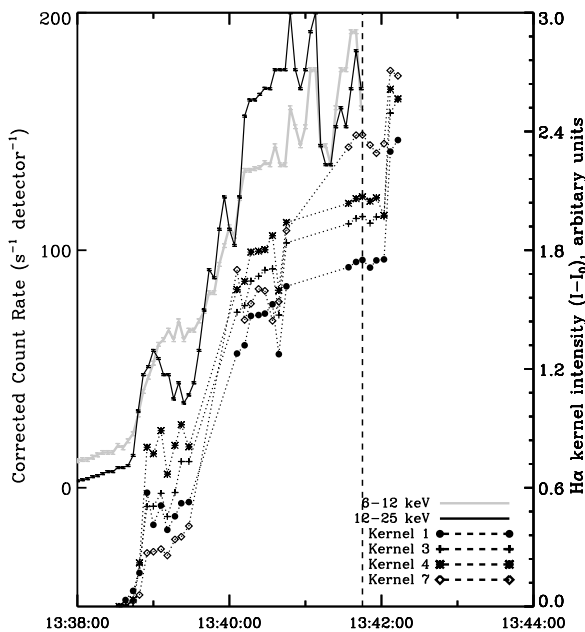
2.3   Temporal evolution of the main flare event

Since TRACE instruments have a higher spatial resolution, the TRACE 195 Åimages are used for the precise identification of the flaring loops elongation and the locations where the loops are likely to be embedded into the photosphere. This provides further information about the loop connectivity in the corona. Temporal evolution of the flaring loops are shown in the right panel of Figure 5. The loops were brighter at 13:40:48 UT (image TRACE 195 Å) at the maximum of hard X-ray emission that was followed by a rather complex loop structures appeared at the moment 13:41:38 UT when HXR emission started to decrease.

A superposition of the HXR sources (dashed and solid contours), Hα emission kernels with the TRACE images in 195 Å and 1600 Å is presented in Figure 5. We used the HXR source images for 12-25 keV and 25-50 keV bands were reconstructed with the PIXON algorithm (Puetter and Pina 1994; Metcalf *et al.* 1996) because of a more sharp shape of the sources. Correct positions of the sources were confirmed by a comparison of the images reconstructed by both CLEAN and PIXON algorithms.

2.3.1   *Magnetic field variations*

For the analysis of a magnetic structure of the flaring region SOHO/MDI magnetograms obtained with 1 minute cadence are used. Figure 6 (left panel) shows the longitudinal magnetogram at 13:40:02 UT over-plotted with the locations of Hα emission kernels. The Hα sources appeared at the op-

tensity images are obtained for the given period of time. As a result, the intensity changes are found in a few bright kernels which appeared at the following times: 1 – 13:38:38 UT; 2 – 13:38:44 UT; 3 – 13:38:49 UT; 4 – 13:38:55 UT; 5,6,7 – 13:40:06 UT; 8,9 – 13:40:45 UT; 10 – 13:41:40 UT. These fast changes in the chromospheric emission are the good spatial indicators of the locations where the initial energy detected from HXR spikes is deposited in the lower atmosphere.
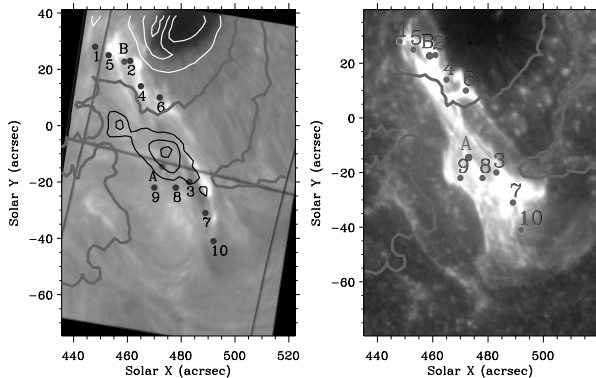
Figure 6. *The left panels shows the 1600Å image at 13:40:02 UT with the locations of Hα emission (kernels) marked by white dots. "A" and "B" show location of pre-flare kernels. The right panels shows the same Hα kernels (black dots) overlaid on the Hα-line image. The black and white contour are negative and positive magnetic fields, correspondingly. A magnetic inversion line or neutral magnetic line (MNL) marked by grey line on both panels.*

posite sides of the neutral magnetic line (MNL), which, in turn, coincides with the filament location (Figure 6, right panel).

From the 1600 Å images by TRACE (Figure 5) and the magnetic field locations (Figure 6) one can see that the flare under investigation was, in fact, a two ribbon flare. One of the ribbons is associated with the HXR sources but the other is not. The ribbons are located on the opposite sides of the inversion line, or magnetic neutral line (MNL), that coincides with the filament (Figure 6, right panel). This points out onto a set of loops embedded into the photosphere from the opposite sides of the MNL with a strong shift of the embedded locations with the opposite polarities strongly elongated with respect to the MNL.

In a few footpoints the HXR sources appear simultaneously (within the observational cadence of 5 seconds) with the Hα kernels while in the other footpoints Hα emission is not associated spatially with HXR sources and appear 10-20 seconds later than any HXR sources in the other locations.

2.3.2 Morphology of flaring kernels in the main event

The spatial locations of the HXR sources and Hα sources towards the MNL and their temporal variations often indicate the sites of energy deposition associated with a magnetic reconnection and transport of this energy into deeper atmospheric levels by high energy particles (Priest and Forbes 2000). The magnetic reconnection events (MRs) are likely to occur in succession in each loop along the ribbon (Priest and Forbes 2000).

Particle (electrons and protons) accelerated during this reconnection precipitate downwards into the loop legs losing their energy in collisions with the ambient particles (Brown 1971) and Ohmic losses in the electric field induced by particles themselves (Zharkova and Gordovskyy 2005a, 2006). This process produces HXR emission from the corona and chromosphere and Hα emission in the chromosphere while the thermo-conduction transfers (via a hydrodynamic response) heating by the beam to the whole atmosphere. Moreover, in the footpoints with HXR emission there are the signs

of a transient increase, or reversible changes, of its magnetic field (Zharkova et al. 2005) which are likely to be caused by the precipitating electrons (van den Oord 1990).

The magnetic field changes recorded for this flare along with the variations of the measured HXR photon flux are presented in Figure 7 with a close-up plot of the spectral index variations at lower energies (< 40 keV) and the electron flux corrected for Ohmic energy losses. This shows that the line-of-sight (LOS) magnetic field changes were definitely associated with the flare phenomena revealing the magnetic flux increase in a close temporal correlation with the variations of the HXR photon flux. However, the cadence of magnetic field measurements was one minute meaning these variations can only show us the magnetic field variations on the scale larger than 1 minute. Thus, the LOS magnetic flux flux shows a steady growth during the flare bursts while only for the third burst at about 13:40:48 UT there is a noticeable magnetic field reduction (up to 26 G/pixel) resembling the reversible 'transient' changes of magnetic field reported by Zharkova et al. (2005). The discussion about a relationship between a magnitude of this transient magnetic field and the electric field induced by precipitating electrons is presented in the section 2.4.

The temporal and spatial patterns of HXR and Hα emission observed in this flare can be indications of the locations of elementary energy releases occurred during a chain of reconnection processes and particle precipitation in each loop which form the two ribbons. However, different temporal correlation (1 second and 10-20 seconds) of HXR and Hα in these loops can possibly, indicate the different kinds of particles precipitating into the opposite loop legs, or namely, electrons and protons being separated into the opposite legs of the same loop (Zharkova & Gordovskyy 2004). This separation results in a few HXR sources to coincide with the Hα kernels appearing on the east side from MNL (where electrons precipitate) and the other set of Hα kernels appearing in the opposite footpoints on the west side (where protons precipitate). This assumption can be tested for both pre-flare and main flare events by comparing the simulation of HXR and Hα emission caused by particle beams with those observed.

2.3.3 Correction of the HXR photon energy flux for Ohmic losses

The parameters of the electron beam energy distribution can be obtained from the RHESSI photon energy spectrum by using the imaging spectroscopy method (Aschwanden *et al.* 2004) which works as follows. The image for each energy bin of the spectrum is reconstructed by using the PIXON algorithm known to have a high photometric accuracy (Puetter and Pina 1994; Metcalf *et al.* 1996). Then we count the photons in each image build for different energy bins and plot their numbers as a function of energy of the relevant bin which presents the observed HXR spectrum. Normally, this spectrum is power-law with the spectral index (γ) and lower energy cutoff of 20 keV. Then the initial energy flux of an electron beam is deduced from the area under the HXR photon curve from the energy 20 keV to the upper energy observed. And the spectral index of beam electron is smaller by one than that of the HXR photon energy spectrum (Brown 1971).

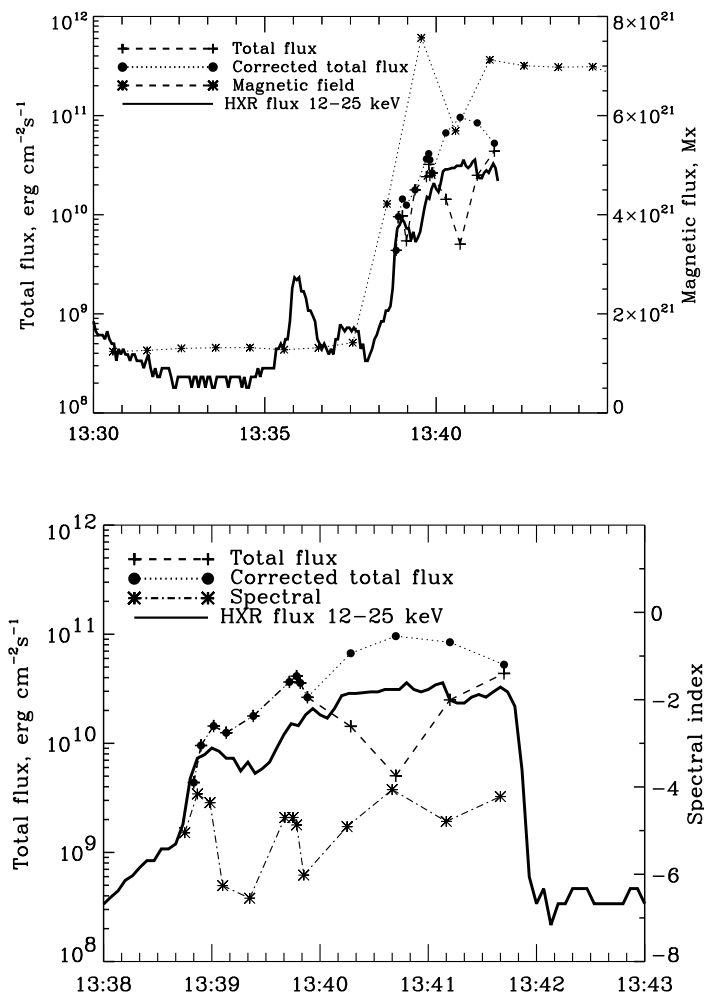6   *V. V. Zharkova, L.K.Kashapova, S.N.Chornogor and O. V. Andrienko*

Figure 7. *Upper plot: The initial electron energy fluxes (the dashed line with pluses), magnetic flux variations (the dot-dashed line with asterisk), the energy fluxes of beam electrons corrected for the induced electric field losses (the dotted line with black disks) in the main flare event are plotted versus the light curve in the energy band of 12-25 keV (the solid curve). Lower plot: The close-in plots of the same initial electron energy fluxes and the electron flux corrected for the induced electric field losses based on the variations of spectral indices of HXR photon spectra at lower energies below 40 keV (the dot-dashed line with asterisk) in the main flare event. The solid line presents the light curve in the energy band of 12-25 keV.*

However, more powerful flares often reveal the elbow-type power law energy spectra models with the two spectral indices: a lower one at the energies below 50 keV and the higher one at the energies above 50-70 keV. These double power law photon spectra are shown to be produced by powerful electron beams if their energy losses during precipitation include not only Coulomb collisions but also Ohmic losses in the electric field carried by beam electrons (Zharkova and Gordovskyy 2006; Zharkova *et al.* 2010). In this case the electric field of the beam leads to a photon spectrum flattening at lower energies and much lower energy flux
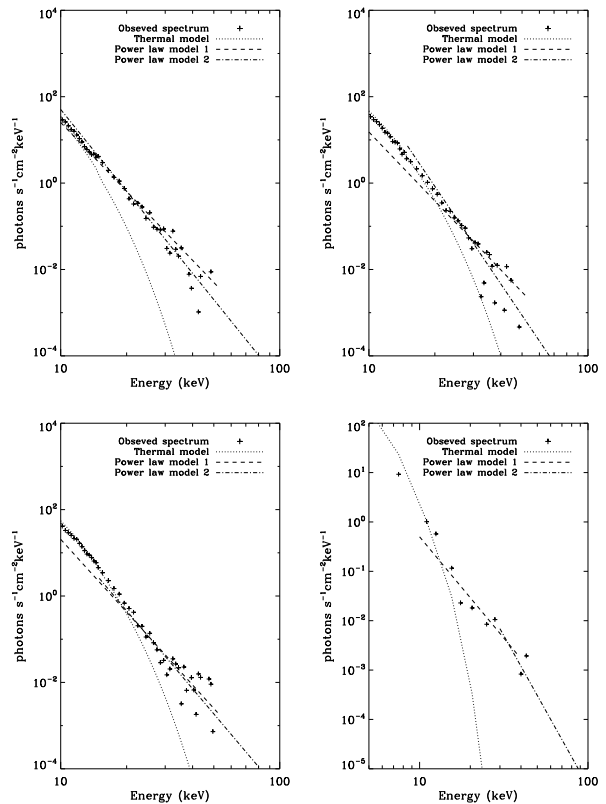

Figure 8. The main flare event: HXR photon energy spectra obtained for the first and third HXR bursts in the energy bands from 12 to 70 keV. The integration times cover: the first burst at 13:38:52-13:38:56 UT (top left plot), 13:38:56-13:39:00 UT (top right plot), 13:39:00-13:39:04 UT (bottom left plot) and the third burst at 13:40:38 UT with the integration time **of 4 s** (bottom right plot). The fitting of the thermal part into the deduced energy spectra at energies below 30 keV carried by taking into account albedo effect is shown in each plot by dotted line (see discussion in the text).

deduced from the elbow-type photon spectrum than those from the single power law one.

A partial ionization degree can contribute to HXR spectrum flattening at lower energies (Kontar *et al.* 2002; Su *et al.* 2009); however, this effect is already considered in our Fokker-Planck (FP) approach applied for the calculation of the electron beam and HXR parameters (Zharkova *et al.* 2010). This is treated via the coefficient for frequency of collisions which varies with depth as per the simulations of hydrodynamic atmospheres (Zharkova and Zharkov 2007) which, in turn, calculates the variations of the ambient plasma ionization with depth. In fact, in our model there are about 70 points in depth of the chromosphere and photosphere having a partial ionization degree which can cause a small HXR spectrum flattening that exceeds those considered by either of Kontar *et al.* (2002); Su *et al.* (2009). Furthermore, in our Fokker-Planck approach (Zharkova *et al.* 2010), unlike the previous authors, we consider relativistic HXR cross-sections which are proven to provide the most correct HXR photon spectra (Kontar *et al.* 2006).

Therefore, the spectral flattening in HXR photon spectra found from the proposed FP approach is produced by
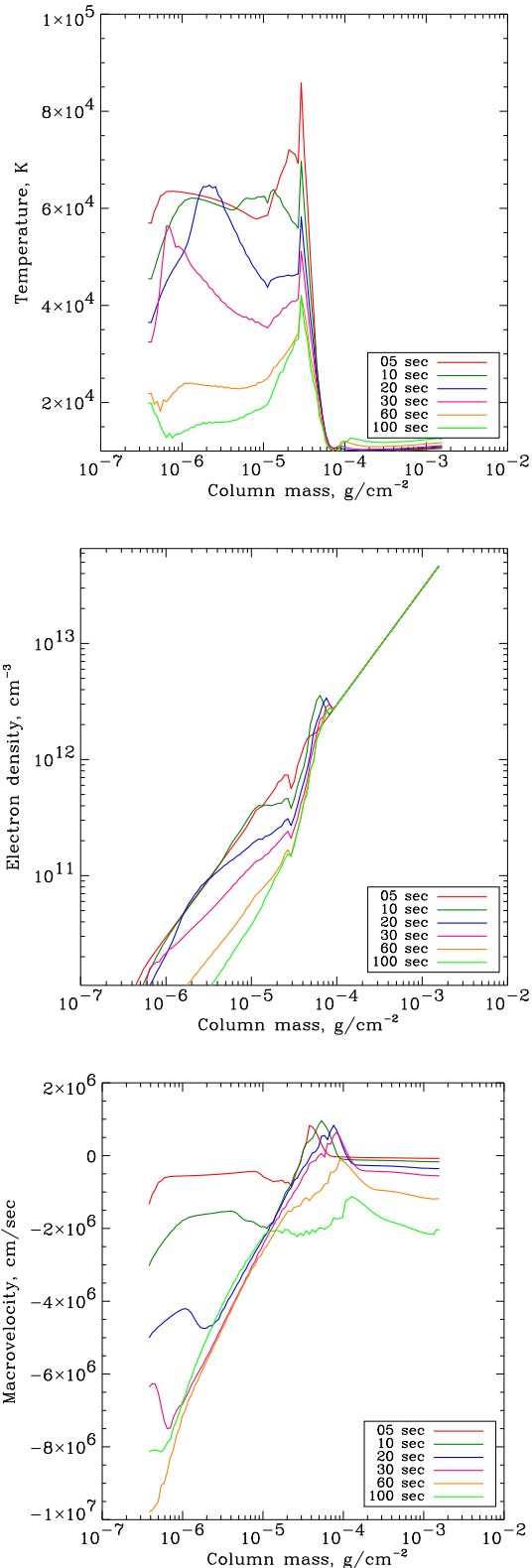
1
2
3
4
5
6
7
8
9
10
11
12
13
14
15
16
17
18
19
20
21
22
23
24
25
26
27
28
29
30
31
32
33
34
35
36
37
38
39
40
41
42
43
44
45
46
47
48
49
50
51
52
53
54
55
56
57
58
59
60

Figure 9. Temperature, density and macro-velocity variations calculated from a hydrodynamic response to the injection of an electron beam in the pre-flare event with the parameters presented in § 2.4.1.

the joint effects of Ohmic losses and partial ionization that is already accounted for in the simulated differences in spectral indices (Zharkova and Gordovskyy 2006). Then, in order to deduce an electron spectrum from the HXR photon one, one needs to keep in mind that the beam electrons emitting these photons have a single power law with the index equal to the spectral index at upper energy as per Fokker-Planck simulations (Zharkova and Gordovskyy 2006),. Then, the correct initial energy flux of beam electrons is deduced by extending a higher energy elbow of the photon spectra back to lower energies and by measuring the area under the new, extended, photon energy spectrum.

Since the difference between the lower and upper spectral indices is dependent on the initial energy flux of beam electrons (Zharkova and Gordovskyy 2006) this photon spectrum flattening can explain the soft-hard-soft variations of the photon spectra observed in some flares by the increase of the initial flux of electron beam from low to high energy and back to low one again, e.g. by a peak in the HXR photon light curve. This method is used for deduction of the spectral index and initial energy flux of beam electrons from their HXR photon spectrum.

2.4   Electron beam parameters

2.4.1   The pre-flare event

During the pre-flare event electron beams are expected to be the sources of the energy delivered to the chromospheric emission in Hα because of a very close temporal and spatial correlation with HXR emission caused by power law beam electrons and the absence of noticeable thermal emission. The HXR photon energy spectrum for the pre-flare event was deduced from the PIXON images obtained in the bands from 12 to 70 keV for the time range in 13:35:53–13:35:57 UT. According to the spectrum fitting procedure, a non-thermal part of HXR photon spectrum for the pre-flare event is fitted by a single power law with the spectral index γ of 3.18 and the total flux of 2.43×10^9 erg s^{-1}cm^{-2}.

Since the photon energy spectrum for this event has a single power law, thus, the beam precipitation was not be affected by the electric field induced by the beam itself, because the latter was relatively weak (Zharkova and Gordovskyy 2006). Hence, the spectral index of beam electrons causing this HXR emission has to be higher by a unity than those of HXR photons as the latter are produced by pure Coulomb collisions (Brown 1971; Zharkova and Gordovskyy 2006).

2.4.2   The main flare event

The main flare event reveal a sharp increase of hard X-ray emission (HXR) at lower energy bands which started at 13:38:48 UT and followed by a slower steady growth until 13:42:00 UT. On top of this steady increase, there are a few steep HXR bursts: the first one with a maximum at about 13:39:00 UT followed by the second and third bursts lasting for about 3 minutes with the maximums for the second one at 13:39:48 UT and the third one at 13:40:38 UT. Then there were few another spikes occurred after 13:41:00 UT at the intensity level slightly higher than the second and third bursts (see Figure 4). The microwave and Hα line emission

8   *V. V. Zharkova, L.K.Kashapova, S.N.Chornogor and O. V. Andrienko*

followed the same temporal patterns that was used to verify a significance of the chosen HXR bursts (see Figures 1 and 4).

The HXR energy spectra in the first three bursts of the main flare event are obtained by building HXR images with the PIXON algorithm for the energy bands from 10 to 70 keV for the first burst (there were not sufficient photons above 70 keV) and from 10 to 100 keV for the second and third ones. The integration time used is dependent on the photon counts in each peak. Because of a lack of photons in the very first burst, only the images can be produced at the maximum of this HXR burst and shortly after it with the integration time of 4 s for all moments. The spectral indices for the energies lower than 50 keV and those for higher energies derived from these PIXON images are summarized in Table 1 and Figure 7, bottom plot.

Hence, the HXR photon energy spectra are restored from the RHESSI observations between 12 and 70 keV for the first burst (1-4 lines in Table 1, Figure 8, the upper and the left lower plots) and the other two bursts from the prolonged HXR emission increase (6-8 and 10-13 bottom in Table 1 and Figure 8, lower right plot for the burst three). The energy spectra vary from a single power law at the start of the each burst to a double (elbow-type) power law at the burst maximum with the spectral index (2nd column in Table 1) changing the slopes at the energies above and below 40 keV as follows: from 6.0 to 5.3 for the first burst maximum, from 6.2 to 4.7 in the second burst and from 6.2 to 4.0 in the third burst.

During each bursts the total energy fluxes integrated from these HXR double power-law photon spectra measured from the RHESSI (3rd column in Table 1) show the flux temporal profiles 'high-low-high' (see Figure 7, bottom plot and all plots in Figure 8) with the 'low' photon flux patterns appearing when the photon spectral indices γ_1 have minimums while the 'higher' patterns appearing where photon spectral indices γ_1 have maximums. As result, the variations of energy spectra in the bursts 1-3 reveal the classic 'soft-hard-soft' profiles in the spectral index change at lower energies (Grigis, Buser, and Benz 2005).

If the photon spectrum is a reflection of the emission produced by beam electrons then to explain it one needs to find a source of two electron beams with different parameters precipitating simultaneously into footpoints. However, a more natural explanation comes if these double power law photon spectra are produced by a single electron beam loosing its energy in Coulomb collisions and Ohmic losses in the electric field induced by the electron beam itself. This allows to explain a reduction of the observed HXR photon flux by the effect of additional photon anisotropy gained in Ohmic losses which affects mostly lower energy electrons, thus reducing their spectral index (Zharkova and Gordovskyy 2006). The higher is the total flux of beam electrons the smaller becomes the spectral index at lower energy (< 70 keV), while the spectral index at higher energies remains unchanged. At the same time, this approach allows to reduce a total number of precipitating electrons because of recycling the same electrons via a return current.

Thus, in general, the dependence of a photon spectral index on the magnitude of a self-induced electric field explains rather naturally a decrease of HXR spectral index at lower energies by an increase in time of the initial energy flux of beam electrons towards the flare maximum followed by its decrease afterwards, similarly as it is observed in the HXR bursts from Figures 4 and 7. In this case the beam which energy flux is increased (like at the burst maximum) will produce much higher self-induced electric field leading to a stronger flattening of the photon spectrum at lower energies. The higher the beam's energy flux the stronger the flattening that is exactly what is presented in Table 1 at the times of the three bursts discussed above.

In order to deduced the total energy flux of a single electron beam producing the observed HXR spectrum, the flux measured by RHESSI from the photon spectra needs to be corrected for Ohmic losses in the self-induced electric field as shown Figure 7) with the *turning points at $\sim$ 38–39 keV by using* the dependences of spectral indices on the initial fluxes presented in Figure 12 in the paper by Zharkova and Gordovskyy (2006). Basically, the photon spectra from Fig. 8 are straightened about the turning point (where the elbow is formed) to match the spectral index of the higher energy part. This allows to increase the total electron energy fluxes where the photon spectral indices are the lowest (see 4th column in Table 1 and Figure 7).

As seen in Fig. 7, the initial energy fluxes of photons (the dashed line with pluses) have smaller decrease in the first burst and much larger ones in the second and third bursts. Thus, a smaller correction of the energy flux for beam electrons is required for the first burst and much larger one for the second and third bursts. where the lower energy spectral indices are strongly decreased ('high-low-high' profile, see the dot-dashed curve with asterisks) at the times when HXR photon flux obtained from the light curves is increased ('low-high-low' profile). The HXR energy flux deduced from PIXON images and corrected for electric field effect with the turning the energy spectrum around the turning point(plotted by the dotted line with black dots), which is assigned to the energy flux of beam electrons, has now the temporal profile 'low-high-low' similar as it is observed in HXR light curves in Figs. 4 and 7.

Although turned out that for the first burst the flux variations had fine temporal variations within a few tens of seconds after its start. The spectral indices were derived more accurately for the first burst as shown in Figure 8 and summarized below. For the time interval 13:38:52 - 13:38:56 UT the lower energy spectral index was $\gamma_1 = 5.3$ and the upper energy index was $\gamma_2 = 6.3$, the kinetic electron temperature of the ambient plasma (by taking into account the albedo effect) was $T_e = 24$ MK and the emission measure EM$=4.3 \times 10^{46}$ cm^{-3}. For the time interval 13:38:56 - 13:39:00 UT the lower energy spectral index was $\gamma_1 = 5.6$ and the upper energy index was $\gamma_2 = 6.0$, the kinetic electron temperature of the ambient plasma was $T_e = 30$ MK and the emission measure EM $= 3.0 \times 10^{46}$ cm^{-3}. For the time interval 13:39:00 - 13:39:04 UT the lower energy spectral index was $\gamma_1 = 5.3$ and the upper energy index was $\gamma_2 = 6.3$, the kinetic electron temperature of the ambient plasma was $T_e = 29$ MK and the emission measure EM $= 4.0 \times 10^{46}$ cm^{-3}. This shows that the first burst had two sub-bursts with the first sub-maximum at 13:38:54 UT and the second one at 13:39:02 UT.

Therefore, we need to assume that the higher energy spectral index was rather high (about 6 for photons as per column three in Table 1) leaving fewer photons with higher

energies to register while the initial energy flux was increasing when the lower energy spectral index decreased to 5.3 or even to 4.1. Only the electron beam with the index 6 and the initial energy flux of about $4.8 \times 10^{10} \ erg \cdot cm^{-2} s^{-1}$ can produce a strong increase of the electron kinetic temperature derived in Figure 8, upper plot, which is caused by a hydrodynamic response to the injection a beam with the spectral index of 5. The variations of temperature versus the beam parameters will be also discussed later when compared with the simulated hydrodynamics in section 3.3. Also estimated parameters of the beams were used for the simulation of their pitch angle distributions at various times, in order to evaluate the induced magnetic field of a transient type induced by such the beams in the ambient plasma (van den Oord 1990).

2.4.3 Magnetic transient in the main flare event

As it is seen in Figs. 4 and 7 for the main flare event, there is a steady increase of the photon flux assuming a steady electron beam injection. This will result in a slowly increased electric field induced by beam electrons. However, on the top of this steady increase there are also fast photon flux bursts (one and two) seen occurring within a few tens of seconds and a few minutes (burst three), supposedly caused by a fast increase of the beam energy fluxes. Thus, during these bursts the electric field induced by beam electrons and indicated by the difference of spectral indices at the lower and higher energies can also increase with the similar temporal profile and its derivative is to be accountable for the transient magnetic field.

From the difference (about 2) of the photon spectral indices at higher and lower energies in the burst three and from a magnitude of the initial energy flux increase (from 2×10^{10} to $9.8 \times 10^{10} \ erg \cdot cm^{-2} s^{-1}$) one can deduce the induced electric field reaching about $\Delta E_b \simeq 3.4 \times E_D$ where E_D is a local Dreicer field (Zharkova and Gordovskyy 2006). In the burst one for which we simulate Hα emission the difference of lower and upper energy indices was about one that indicates not a very strong induced electric field of $\Delta E_b \simeq 0.2 \times E_D$ on the top boundary. High energy electrons with energies above 100-200 keV can reach the upper photosphere and gain at the same time a very anisotropic distribution in pitch angles (Zharkova *et al.* 2010) making them moving across the loop. These electrons become spread over a certain height of the loop leading to a fast change of the induced electric field in depth as plotted in Figure 1 of (Zharkova and Gordovskyy 2006) and in time, according to the temporal profile of the three bursts plotted in Figure 7.

Then from the motion equation of precipitating electrons one can derive that $\frac{1}{c}\frac{\partial \vec{B}}{\partial t} = -\nabla \times \vec{E_b}$ where $\vec{E_b}$ is the electric field induced by these electrons, c is the speed of light (in CGS units). For the electron beam distribution function relevant for this flare (see § 2.4.2 about a presence of the self-induced electric field), this will result in the transient LOS magnetic field induced by those beam electrons which move in the ambient plasma perpendicular to the loop's LOS magnetic field (van den Oord 1990). This induced, or transient, magnetic field has the polarity opposite to those originally present in this footpoint before the flare. Thus, this additional magnetic field can be seen as a magnetic field reversal

in the MDI magnetogram taken at the time close to the HXR maximum which disappears after the beam's cutoff as often observed in flares (Kosovichev and Zharkova 2001; Régnier and Fleck 2004; Zharkova et al. 2005; Sudol and Harvey 2005). The magnitude of this 'transient' magnetic field can approach about $30 - 100$ G at its maximum that is often observed in flares with the magnetic measurements of MDI or GONG (Zharkova et al. 2005; Sudol and Harvey 2005).

The variations of a magnetic field in the main flare compared to HXR flux in Fig. 7 show some evidences of a presence of the induced magnetic field in the peak 3 which lasted more than 2 minutes. But there are no much variations in the peaks 1 or 2 which lasted under or about a minute. We established in Figs. 7 and 8 that the HXR photon spectra for the peak 1 have mild flattening towards lower energies discussed above. Therefore, in order to evaluate a transient magnetic field in the peak 1 we need a much better (a few seconds) cadence of magnetic field variations which is not yet available. Although, the estimations of this electric field made from the difference of HXR spectral indices at lower and higher energies was performed a few paragraphs above.

For the peak 3 one can deduce the magnitude of the transient magnetic flux (about 2×10^{21} Mx, or 26 G/pixel), so theoretically, can also evaluate the induced electric field from the Faraday's equation above. However, we do not have the measurements of the loop size where the magnetic field changes occurred. Instead we could estimate from simulations of electron distribution functions the heights in the loop where the bulk beam electrons (with lower cutoff energy) starts moving across the loop. This motion when it approaches the upper photosphere depths can lead to the observed temporal variations of a magnetic field seen as the transient.

Thus, the problem is strongly non-linear and require to have a high resolution measurements of HXR emission in high energy bands, in order to reach lower atmospheric levels which we do not have for this flare. Also we cannot estimate a number of electrons moving in the two directions perpendicular to the vertical since we do not yet simulate electron beam precipitation with a 2D-3D time-dependent Fokker-Planck equation during such the prolonged injection for 2-3 minutes occurred in the third burst. This study can be done in another paper after the modification of Fokker-Planck code.

3 MODEL SIMULATIONS AND DISCUSSION

3.1 Description of the theoretical models

Now let us try to interpret the simultaneous temporal variations of hard X-ray and Hα emission related to the first burst (full line intensity only because the Hα line profiles were not observed). In order to reproduce the hydrogen emission in a flaring atmosphere heated by electron beams injected from the reconnection site on the loop top, the four approaches are considered: particle acceleration, particle precipitation, ambient plasma hydrodynamics and radiative approach for hydrogen atoms including the outcomes from all the above models.

10   *V. V. Zharkova, L.K.Kashapova, S.N.Chornogor and O. V. Andrienko*

Table 1. *The temporal evolution of the HXR photon spectra: time (the first column), spectral indices $\gamma 1$ in the lower energy range of 12–39 keV (the second column),spectral indices $\gamma 2$ in the energy range of 39–100 keV (the third column) and total fluxes before (the fourth column) and after (the fifth column) the correction for Ohmic losses in a self-induced electric field (Zharkova and Gordovskyy, 2006).*

Time (UT)	$\gamma 1$	$\gamma 2$	Total flux, $erg/cm^2 s^{-1}$	Corrected total flux $erg/cm^2 s^{-1}$
13:38:40–13:38:50	-5.1	n/a	4.4×10^{09}	4.4×10^{09}
13:38:50–13:38:54	-4.2	n/a	9.6×10^{09}	9.6×10^{09}
13:38:57–13:39:01	-4.4	n/a	1.4×10^{10}	4.8×10^{10}
13:39:04–13:39:08	-5.3	-6.3	1.3×10^{10}	2.9×10^{10}
13:39:19–13:39:23	-6.6	-6.6	1.8×10^{10}	1.8×10^{10}
13:39:38–13:39:43	-4.7	-6.1	3.7×10^{10}	5.1×10^{10}
13:39:43–13:39:47	-4.7	-6.0	4.1×10^{10}	7.1×10^{10}
13:39:45–13:39:49	-4.9	-6.0	3.6×10^{10}	5.6×10^{10}
13:39:49–13:39:53	-6.0	-6.0	2.6×10^{10}	2.6×10^{10}
13:40:13–13:40:17	-4.9	-6.0	1.4×10^{10}	6.7×10^{10}
13:40:38–13:40:42	-4.1	-6.0	5.0×10^{09}	9.6×10^{10}
13:41:08–13:41:12	-4.8	-6.0	2.5×10^{10}	8.4×10^{10}
13:41:38–13:41:42	-4.2	-6.0	4.4×10^{10}	5.3×10^{10}

3.1.1   Particle kinetics and HXR emission

Let us assume that the HXR emission is produced by beam electrons injected into loop legs from a magnetic reconnection site on the loop top as a standard flare model (Zharkova *et al.* 2010). In this case, electrons and protons are accelerated during a magnetic reconnection to very high energies (Zharkova & Gordovskyy 2004) while gaining power law energy spectra with either similar spectral indices, if the guiding field is strong, or with the spectral indices of protons being 1.5 times lower that those of electrons (Zharkova and Gordovskyy 2005b). Also for the topologies with a strong guiding field the electrons and protons can be separated into the opposite footpoints of the same loop interacting with another loop (Zharkova & Gordovskyy 2004; Zharkova & Agapitov 2009). The electrons and protons accelerated during a magnetic reconnection process gain different velocities at ejection from a current sheet which are by 1.5 orders of magnitude lower for protons than for electrons (Zharkova & Gordovskyy 2004; Zharkova & Agapitov 2009).

Thus, we calculate the kinetics of electron beams injected from the atmosphere top and precipitating downwards in collisions and Ohmic losses by using a Fokker-Plank approach (Siversky & Zharkova 2009) and using the acceleration model solutions above as the boundary condition on the top boundary. Then the heating of the ambient plasma by beam electrons injected stationary during 20 s into the previously heated atmosphere is computed for collisions and Ohmic energy losses (Gordovskyy *et al.* 2005). The electron energy flux is assumed to have a triangular temporal profile.

3.1.2   Hydrodynamics of the ambient plasma

Then by using these heating functions the hydrodynamic responses of a two–temperature plasma (electrons and ions) heated by beam electrons are calculated. These include, similar to the approach by Somov et al. (1981) the two energy conservation equations (for electrons and ions), the momentum and beam kinetic equations with the heating being provided either by electron or proton beams (Zharkova and Zharkov 2007; Somov et al. 1981). The energy losses include the optically thin radiative losses in all the lines of the coronal plasma with the solar abundance (McWhirter*et al.* 1975) and radiative losses in optically thick hydrogen lines and continua (Kobylinskij and Zharkova 1996). The hydrodynamic solutions are obtained for every second after a beam onset and the derived temperature, density and macro-velocity variations and their detailed description was presented in Zharkova and Zharkov (2007).

This approach allows to simulate not only a strong increase of the temperature in the corona caused by the chromospheric evaporation reported by many other hydrodynamic simulations (Fisher and *et al.* 1985) of observed in blue shifts of soft X-ray and UV lines (see for example Antonucci *et al.* 1982) but also a formation of low temperature condensation at the lower chromosphere travelling as a shock towards the photosphere and observed with red shifts in Hα and other chromospheric lines (see for example Canfield *et al.* 1984; Ishimoto and Kurokawa 1984). This shock is exactly the region in a flaring atmosphere where Hα emission origins which observations often reveal well observed red shifts. For a further discussion of the hydrodynamic approach we refer to our paper (Zharkova and Zharkov 2007) and the references therein.

3.1.3   Radiative transfer of hydrogen emission

Now these hydrodynamic models combined with particle kinetics used for calculation of collisional rates by both thermal and non-thermal electrons are used as the input physical model for the radiative simulation of the full-non-LTE radiative transfer of hydrogen emission in the main Lyman and Balmer lines and continua. In this paper we are only interested in simulating the full Hα intensities in the kernels (because of lack of line profile observations) associated with the increase of HXR intensity and comparing the effects of thermal and non-thermal excitation and ionization, we will concentrate on the temperature and density variations of model atmospheres but leave out the consideration the effects related to macro-velocities of the ambient plasma.

In the radiative model, let us solve the system of radiative transfer (where appropriate) and steady state equations for 5 level plus continuum hydrogen atoms considering the radiative transfer equations in all Lyman and Balmer lines and their continua (Zharkova & Kobylinskij 1991, 1993). The ambient temperature and densities are taken from the hydrodynamic models above. The following mechanisms of atom excitation and de-excitation are considered: radiative by external radiation from the chromosphere and photosphere and by diffusive radiation produced by radiative transfer, by thermal collisions with the ambient electrons and by non-thermal collisions with beam electrons or protons. The hydrogen non-thermal excitation and ionization rates were calculated analytically from the formulae by Zharkova & Kobylinskij (1993) obtained for hydrogen emission cross-sections and beam electron distributions from the continuity equation (Zharkova & Kobylinskij 1989).

The non-thermal excitation and ionization are shown to dominate thermal collisional ones at chromospheric depths

for the first 20 seconds before the plasma is heated by thermal conduction (Zharkova & Kobylinskij 1989, 1991) meaning that at the flare onset the non-thermal radiative processes dominate and cause very strong excitation and ionization of the ambient hydrogen which is nearly 90% of the ambient plasma. Also it has to be noted that the non-thermal rates above have a smooth distribution (decrease) with the atmospheric depth defined by the density decrease of beam electrons derived from the continuity equation.

This is significantly different from the non-thermal excitation and ionization rates used in the other simulations (see for example Kašparová *et al.* 2005a) which were calculated by Aboudarham and Henoux (1987) using for a beam density the one derived from the beam flux conservation equation (Brown 1971) while our are calculated in the continuity equation approach. The flux conservation electron beam density is significantly over-estimated at the upper chromosphere depth (above the full stopping depth of electrons with the lower energy cut-off). This leads to non-realistic over-heating of the ambient plasma (Mauas and Gomez 1997) and, in turn, leads to a strong over-ionization and over-excitation of the hydrogen at the upper chromospheric level where the Hα core is formed. As a result of this simplification, in the flux conservation approach is reflected in the strong non-thermal collision effect on the Hα core emission unlike with the continuity equation approach used by Zharkova & Kobylinskij (1989, 1991) the effects on non-thermal ionization and excitation is evenly spread in the chromospheric depth becoming more significant at deeper levels where the ambient ionization degree decreased to 10^{-6} and the effect of non-thermal ionization dominates (Zharkova & Kobylinskij 1991, 1993).

Recent investigation of the physical conditions in flares associated with sunquakes (Zharkova 2008) has revealed that this smooth ionization of the ambient plasma by precipitating electron beams predicted by Zharkova & Kobylinskij (1993) creates the path for faster propagation of the seismic emission throughout the whole flaring atmosphere. This, in turn, creates the visual effect of a 'back-warming heating', or the increase of a number of ambient electrons (defining the ambient ionization degree) well above the LTE magnitudes defined by the Saha equation for a given ambient temperature. Therefore, the non-thermal ionization and excitation plays a significant role in defining the physical conditions in solar flares and needs to be taken into account in any radiative approach.

3.2 Model of the pre-flare event

The temporal variations of full Hα line intensities calculated for the hydrodynamic atmosphere heated by the electron beam of the pre-flare event B correspond in time to the Hα peaks plotted in Figure 2. However the maxima of the simulated Hα emission are higher than those measured that can be explained by a spatial smearing of the emission in flaring loop which was not considered in the model.

From a presence of the Hα kernel B in the pre-flare event one can conclude that there was the initial energy release of a smaller scale produced by the electron beam with a spectral index of 3.2 and a very moderate intensity about $3 \times 10^9 \ erg \cdot cm^{-2} s^{-1}$. Such the beam does not induce
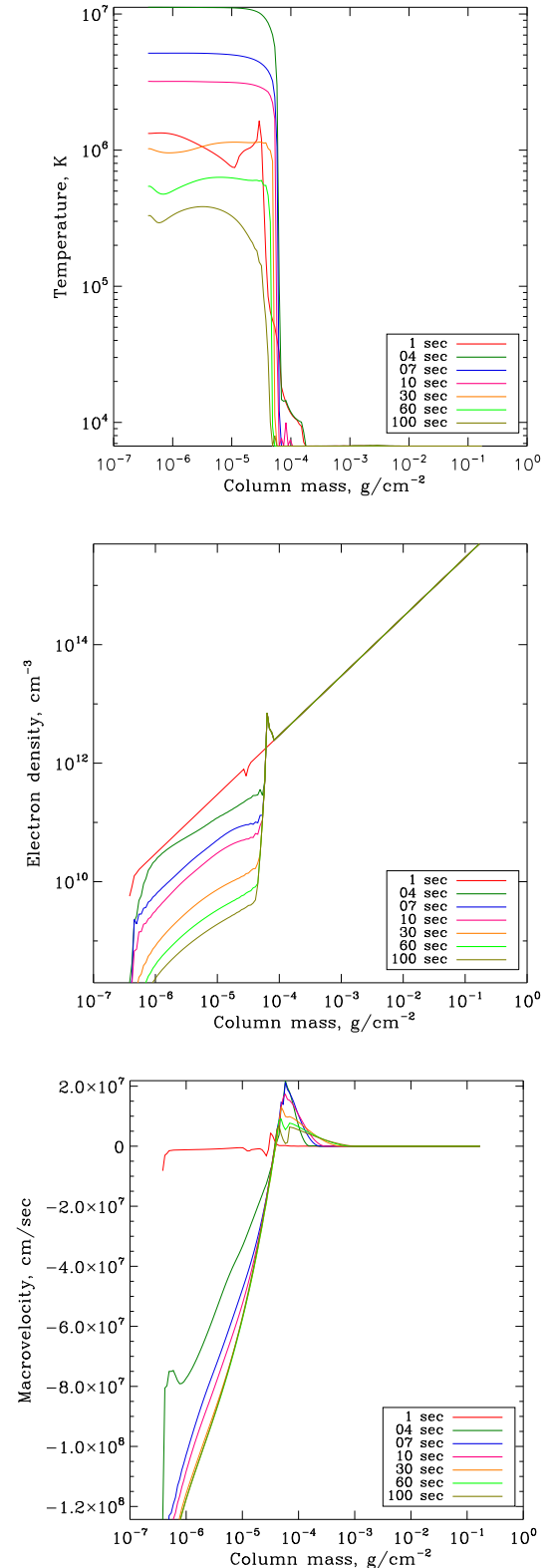

Figure 10. Temperature, density and macrovelocity variations in the main flare event calculated from a hydrodynamic response to the injection of an electron beam with the parameters from the Table 1.

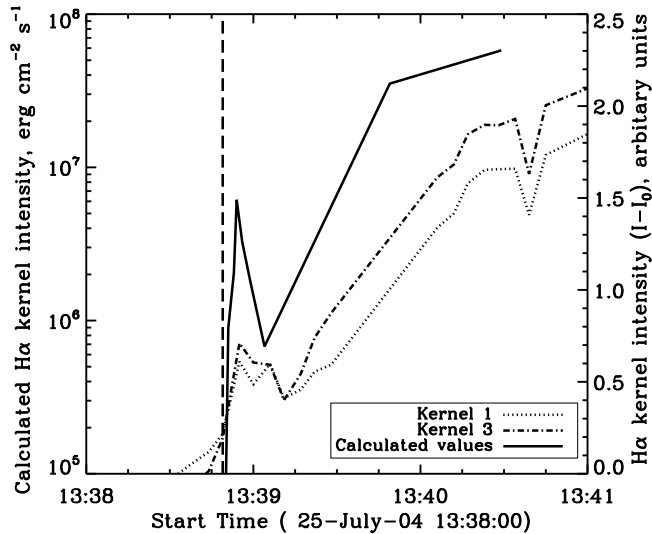12   *V. V. Zharkova, L.K.Kashapova, S.N.Chornogor and O. V. Andrienko*

Figure 11. The temporal variations of the simulated vs calculated Hα line intensity in the pre-flare event.

a significant electric field and, as result, the photon energy spectrum produce by such the has a single power law.

The atmosphere heating by this electron beam is rather mild with the upward velocities of up to 100 km/s and the downward ones being less than 1 km/s, i.e. there is no explosive evaporation of the chromosphere into the corona (see Figure 9), similar to those reported by Allred *et al.* (2005). The lower atmosphere heating is not significant approaching the maximum temperature of 7500K (see the upper plot in Figure 9); also in this case there is no a low-density condensation formed in the chromosphere.

Thus, the observed emission in Hα kernels in the pre-flare event is caused mainly by the excitation and ionization of hydrogen atoms from non-thermal collisions with beam electrons. The beam is rather hard ($\gamma = 3.2$) meaning that the beam electrons can easily reach the lower chromosphere levels and produce the rather low Hα emission observed in the kernel B.

3.3 Hα flare emission in the main flare events

3.3.1 Hydrodynamics of the atmosphere

The main flare events were observed in 10 Hα kernels appearing on the opposite sides from the MNL (see Figure 6) and discussion in § 2.4.2 and § 2.4.3.

Thus, the hydrodynamics of the atmosphere heated at about 11:39:00 UT by an electron beam with the parameters derived in Table 1 and Fig. 8 have to be substantially different from the pre-flare event. The time of the first burst is selected because the observed Hα kernels appeared first at that time. This confirms that the flaring atmospheres in the kernels were not yet heated by beam electrons to high temperatures, so non-thermal processes should dominate the thermal ones. At the later times the atmospheres become already heated by the first beam and keep being further heated by other beams injected at about 11:39:00 UT and 11:41 UT.

If we would use the initial energy fluxes derived from the energy spectra (see Fig. 7) then the hydrodynamics of a flaring atmosphere could be very similar to those simulated for the pre-flare event discussed above. While the fitting of the thermal spectrum into the HXR energy spectrum derived in Fig. 8 reveal the mean electron kinetic temperature to be about 24, 30 and 29 MK for the consecutive intervals of 4 s starting from 13:38:52 UT. This can only be achieved by increasing the initial energy flux of beam electrons with the effect of self-induced electric field and increasing its spectral index to the one (6.2) derived at higher energies. Only in such the way it is possible to fit the observed thermal temperatures, since heating by the beam with the same energy flux but harder spectral indices (4 or 5) produces a smaller increase of the temperature in the corona than those measured in Fig. 8 (top plot).

After the beam onset they heat the ambient plasma so that the ambient temperature increase in the corona of both components (electrons and ions) approaches a few tens MK with the ions' temperature being twice smaller than the electrons' one, while the macrovelocity of the explosive evaporation into the corona reaches 1200 km/s. Although the thermal temperatures derived from these spectra are still higher than those simulated in HD models for the relevant times after beam injection (Fig. 10. This discrepancy has been removed after the albedo effect calculated for isotropic beam (in pitch angles) was excluded since in this flare the electron beams seem to be very anisotropic. As result, the electron temperatures are reduced by about factor two for each moment that allowed them to fit very closely the temperature profiles in the corona simulated for 5-15 seconds after the beam onset.

After the beam is stopped, the ambient plasma continues with a chromospheric evaporation and an increase of the coronal density back to the pre-flare magnitudes while becoming cooled by radiation for another hour or so. Also in the first ten-fifteen seconds a lower-temperature condensation is formed in the chromosphere moving with a supersonic speed towards the photosphere which produces low-temperature optical emission in the first burst of the main event. This condensation is formed in the chromosphere while in the pre-flare event it appeared just below the transition region. It has a much higher temperature up to 10^4 K and a density up to 10^{14} cm^{-2} compared to the pre-flare event (7×10^4 and 3×10^{13} cm^{-2}, respectively) and its macrovelocity approaches 200 km/s. The increased temperature in this condensation defines the timescale of an increase of the contribution by thermal electron impacts on Hα emission which competes with the contribution of non-thermal excitation and ionization by power law electron beams.

3.3.2 Resulting Hα emission

The full Hα intensity and the intensities in all the other hydrogen lines and continua were calculated for the hydrodynamic models obtained for the very first moments of electron beam injection at about 11:38:49 UT. We use a full non-LTE approach for the 5 level plus continuum hydrogen atom (Zharkova & Kobylinskij 1991, 1993). The full Hα line intensities simulated by taking into account a joint effect of radiation, thermal and beam electrons with the parameters derived from HXR spectra and multiplied by the average

kernel area are plotted in Figure 11 (solid curve). The observed evolution of the Hα emission in the kernels 1, 3, 4 and 7 located on the opposite sides from the MNL are plotted in Figure 11 (dashed and dot-dashed curves).

The simulations reveal a sharp increase of the full Hα emission immediately after the onset of an electron beam injection in the second burst taken from Table 1, likely caused by the non-thermal hydrogen excitation by beam electrons (the impulsive phase). A further increase in Hα intensity occurs owing to the temperature growth in the lower chromosphere caused by a hydrodynamic response owing to injection of other electron beams. The observed Hα emission in kernel 1 and kernel 3 qualitatively fits rather well the theoretical emission increase in the impulsive phase starting at 13:38:49 UT. At the same time the Hα emission in the kernels 4 and 7 reveal a delay about 10-20 seconds between the simulated and observed Hα maxima.

This temporal delay combined with the location towards the MNL of these kernels 4 and 7 and the other two kernels 1 and 3 allows us to assume that the emission in them is likely to be caused by non-thermal excitation by different agents rather than by the thermal excitation caused by a hydrodynamic response in the lower atmosphere. In the sources 1 and 3 this emission was caused by beam electrons while in the kernels 4 and 7 this emission has to be caused either the ambient electrons accelerated on plasma turbulence induced by the original precipitating beam (Hamilton and Petrosian 1990) or by the protons accelerated at a magnetic reconnection of the loop as per the acceleration model in a reconnecting current sheet proposed by Zharkova & Gordovskyy (2004).

The secondary acceleration of the ambient electrons on plasma turbulence should occur within a very short timescale of a second or two that obviously, much shorter that the delay in occurrence of Hα emission observed in these kernels. Thus, we need to consider other agents, which are able to excite hydrogen atom to the 3rd state and produce Hα line emission. The good candidates for this process are accelerated protons which also precipitate into loop legs from the top with the velocities by 1.5 orders of magnitude lower than electrons (Zharkova & Gordovskyy 2004). Because of the absence of γ-ray observations for this flare, one can conclude that the protons in this flare did not gain energies higher than a few tens MeVs. Although these lower energy protons can easily produce non-thermal H-α emission as noted by Henoux (1991).

4 CONCLUSIONS

The temporal variations of HXR, radio and Hα emission in this flare revealed two phases: pre-flare and flare events. The main flare showed three major bursts lasting under or one minute (bursts 1 and 2) or up to 3 minutes (burst 3). Magnetic flux variations of the LOS magnetic field were found to closely correlate with the temporal variations of HXR emission, showing a strong transient magnetic field at the time of the third burst.

The flare under investigation was, in fact, the two ribbon flare as can be seen in 1600 Å images by TRACE (Figure 5) while Hα observations show the sequential appearance of the kernels along these ribbons. The one of the ribbons

is found to be associated with the HXR sources while the other is not. The ribbons were located on the opposite sides from the magnetic inversion, or neutral line (MNL), that coincides with the filament (Figure 6, right panel.) This points out onto a set of loops embedded into the photosphere from the opposite sites of MNL which are strongly shifted and elongated to the MNL.

In the pre-flare event there was a brief increase of HXR and Hα intensity observed the kernel B. The theoretical hydrodynamic response of the ambient plasma to the electron beam injection with the parameters derived for the pre-flare event shows a moderate increase of the temperature and density at the chromospheric levels. The electron temperature was found to be about 24-30 MK and the emission measure to vary about $4 \times 10^{46} cm^{-3}$. However, for the best fit of this derived temperature to the temperatures simulated in the hydrodynamic model for the electron beam with given parameters, the correction for the albedo effect using isotropic electron distribution function had to be eliminated. This results in the electron temperatures decrease to about 10MK to 20MK during the first peak of the main flare (13:39:00 UT) fitting very well the hydrodynamic predictions. The Hα intensity variations in the kernel B of the pre-flare event was well fit by the simulations of non-thermal excitation by the electron beam with the parameters derived from HXR emission.

In the first burst of the main flare event occurred at the start of the main flare event (11:38:52 - 11:39:04 UT) there were two types of Hα kernels observed: the first type (called HXR+Hα) associated with HXR emission (kernels 1 and 3, for example) and the second type (kernels 4 and 7, for example) which did not have such the associations. The increase of HXR emission during the first impulse was associated with the beam electrons with the spectral index of 5 and the initial energy flux of $4.8 \times 10^{10}\ erg cm^{-2} s^{-1}$. The initial energy flux of the injected beam was derived from the observed HXR flux by using the correction for Ohmic losses by electron beams with strong pitch angle anisotropy.

The theoretical hydrodynamic model calculated for heating by electron beam with the parameters derived in the burst 1 with the initial flux corrected for the effects of the self-induced electric field can explain the variations of thermal electron temperature (12MK, 15MK, 14.5MK) observed by RHESSI in this first burst if the albedo effect is excluded.

For the first type kernels which appear on the east side from MNL the temporal variations of Hα intensity were well fit by the variations of full Hα intensity simulated for a joint thermal plus non-thermal excitation of 5 level hydrogen atom in the ambient plasma heated via a hydrodynamic response. While in the second type kernels appeared on the west side from MNL, which are magnetically connected to the type one ones, the observed Hα intensity lagged the simulated one by ten or more seconds. The Hα emission delays in the kernels 4 and 7 can be caused by non-thermal excitation by beam protons precipitating in these loop legs since their precipitation time is 10s seconds longer than those by electrons precipitating in the opposite legs.

These differences in the temporal and spatial evolution of HXR and Hα sources towards the MNL are likely to point out to some magnetic topology differences occurred during the flare event. We can speculate that the temporal varia-

14   *V. V. Zharkova, L.K.Kashapova, S.N.Chornogor and O. V. Andrienko*

tions and locations of HXR, Hα and magnetic field sources indicate the magnetic reconnection sites (MRS) occurring in different loops in a succession. If this is the case, then one can speculate that these MRS are assumed to cause the acceleration of electrons and protons and their separation into the opposite loop legs (Zharkova & Gordovskyy 2004; Zharkova & Agapitov 2009). In addition, this scenario can explain the temporal delays of about 10 seconds in Hα emission appearance in the type two kernels compared to those of the type one by the fact that accelerated electrons gain in a current sheet the velocities by the 1.5 order of a magnitude higher than protons (Zharkova & Gordovskyy 2004; Zharkova and Gordovskyy 2005a) thus producing the delayed ambient heating and non-thermal hydrogen excitation in the loops with protons (Zharkova and Zharkov 2007).

REFERENCES

Aboudarham,J & Henoux, J.C., 1987, *Astron. Astrophys.*, **174** , 270.

Allred, J.C., Hawley, S.L., Abbet, W.P. & Carlson, M., 2005, *Astrophys. J*, **630** , 573.

Antonucci, E.; Gabriel, A. H.; Acton, L. W.; Leibacher, J. W.; Culhane, J. L.; Rapley, C. G.; Doyle, J. G.; Machado, M. E.; Orwig, L. E., 1982, *Solar Phys.*, **78** , 107.

Asai, A., Masuda, S., Yokoyama, T., Shimojo, M., Isobe, H., Kurokawa, H., and Shibata, K.: 2002, *Astrophys. J.* **578**, L91.

Aschwanden M. J., Metcalf T. R., Krucker S., Sato J., Conway A. J., Hurford G. J., Schmahl E. J., 2004, *Solar Phys.*, 219, 149

Battaglia M., Fletcher L., Benz A. O., 2009, A&A, 498, 891

Bianda, M., Benz, A.O., Stenflo, J.O., Küveler, G., and Ramelli, R.: 2005, *Astron. Astroph.* **434**, 1183.

Brown, J.C.: 1971, *Solar Phys.* **18**, 489.

Canfield, R. C.; Gunkler, T. A.; Ricchiazzi, P. J.: 1984, *Astrophys. J.* **282**, 296.

Cheng, C.C., Orwig, L.E., and Tandberg-Hanssen, E.: 1987, *Solar Phys.* **113**, 301.

Chornogor, S.N., Kashapova, L.K., Sych, R.A., and Andriyenko, O.V.: 2005, *The Dynamic Sun: Challenges for Theory and Observations* **600**.

Handy, B.N., Acton, L.W., Kankelborg, C.C., Wolfson, C.J., Akin, D.J., Bruner, M.E., Caravalho, R., Catura, R.C., Chevalier, R., Duncan, D.W., Edwards, C.G., Feinstein, C.N., Freeland, S.L., Friedlaender, F.M., Hoffmann, C.H., Hurlburt, N.E., Jurcevich, B.K., Katz, N.L., Kelly, G.A., Lemen, J.R., Levay, M., Lindgren, R.W., Mathur, D.P., Meyer, S.B., Morrison, S.J., Morrison, M.D., Nightingale, R.W., Pope, T.P., Rehse, R.A., Schrijver, C.J., Shine, R.A., Shing, L., Strong, K.T., Tarbell, T.D., Title, A.M., Torgerson, D.D., Golub, L., Bookbinder, J.A., Caldwell, D., Cheimets, P.N., Davis, W.N., Deluca, E.E., McMullen, R.A., Warren, H.P., Amato, D., Fisher, R., Maldonado, H., and Parkinson, C.: 1999, *Solar Phys.* **187**, 229.

Henoux J. C., 1991, AdSpR, 11, 7

Grigis, P.C., Buser, D., and Benz, A.O.: 2005, *Solar Magnetic Phenomena* **320**, 199.

Gordovskyy, M., Zharkova, V.V., Voitenko, Y.M., and Goossens, M.: 2005, *Advances in Space Research* **35**, 1743.

Fisher, G.H., Canfield, R.C. and McClymont, A.N.: 1985, *Astrophys. J.* **289**, 414.

Hamilton, Russell J.; Petrosian, Vahe F: 1990, *Astrophys. J.* **365**, 778.

Henoux, J.C.: 1991, *Advances in Space Research* **11**, 7.

Hiei, E.: 1987, *Solar Phys.* **113**, 249.

Hudson, H.S.: 1972, *Solar Phys.* **24**, 414.

Ichimoto, K.; Kurokawa, H., 1984, *Solar Phys.* **93**, 105.

Kašparová, J., Karlický, M., Kontar, E.P., Schwartz, R.A., and Dennis, B.R.: 2005, *Solar Phys.* **232**, 63.

Kašparová, J., Karlický, M., Schwartz, R.A., and Dennis, B.R.: 2005, *Solar Magnetic Phenomena* **320**, 187.

Kobylinskij, V.A. & Zharkova V.V.: 1996, *Advances in Space Research* **17**, 4-5, 129.

Kontar, E. P., Brown, J. C., McArthur, G. K., 2002, *Solar Phys.*, **210**, 419.

Kontar, E. P., MacKinnon, A. L., Schwartz, R. A., Brown, J. C., 2006, *Astron. Astrophys.*, **446**, 1157.

Kosovichev, A.G. and Zharkova, V.V.: 2001, *Astrophys. J.* **550**, L105.

Kurokawa, H., Takakura, T., and Ohki, K.: 1988, *Publications of the Astronomical Society of Japan*, **40**, 357.

Lin, R.P., Dennis, B.R., Hurford, G.J., Smith, D.M., Zehnder, A., Harvey, P.R., Curtis, D.W., Pankow, D., Turin, P., Bester, M., Csillaghy, A., Lewis, M., Madden, N., van Beek, H.F., Appleby, M., Raudorf, T., McTiernan, J., Ramaty, R., Schmahl, E., Schwartz, R., Krucker, S., Abiad, R., Quinn, T., Berg, P., Hashii, M., Sterling, R., Jackson, R., Pratt, R., Campbell, R.D., Malone, D., Landis, D., Barrington-Leigh, C.P., Slassi-Sennou, S., Cork, C., Clark, D., Amato, D., Orwig, L., Boyle, R., Banks, I.S., Shirey, K., Tolbert, A.K., Zarro, D., Snow, F., Thomsen, K., Henneck, R., McHedlishvili, A., Ming, P., Fivian, M., Jordan, J., Wanner, R., Crubb, J., Preble, J., Matranga, M., Benz, A., Hudson, H., Canfield, R.C., Holman, G.D., Crannell, C., Kosugi, T., Emslie, A.G., Vilmer, N., Brown, J.C., Johns-Krull, C., Aschwanden, M., Metcalf, T., and Conway, A.: 2002, *Solar Phys.* **210**, 3.

Mauas, J.D. & Gomez, O.: 1997, *Astrophys. J.* **483**, 496.

McWhirter, R. W. P.; Thonemann, P. C.; Wilson, R.: 1975, *Astron. Astrophys.* **40**, 63.

Metcalf, T.R., Alexander, D., Hudson, H.S., and Longcope, D.W.: 2003, *Astrophys. J.* **595**, 483.

Metcalf, T.R., Hudson, H.S., Kosugi, T., Puetter, R.C., and Pina, R.K.: 1996, *Astrophys. J.* **466**, 585.

van den Oord, G. H. J., 1990, *Astron. Astrophys.* **234**, 496.

Priest, E. and Forbes, T.: 2000, *Magnetic Reconnection, by Eric Priest and Terry Forbes, pp. 612. ISBN 0521481791. Cambridge, UK: Cambridge University Press, June 2000.*.

Puetter, R.C. and Pina, R.K.: 1994, *Experimental Astronomy* **3**, 293.

Régnier, S. and Fleck, B.: 2004, *SOHO 15 Coronal Heating* **575**, 519.

Ricchiazzi, P.J. and Canfield, R.C.: 1983, *Astrophys. J.* **272**, 739.

Scherrer, P.H., Bogart, R.S., Bush, R.I., Hoeksema, J.T., Kosovichev, A.G., Schou, J., Rosenberg, W., Springer, L., Tarbell, T.D., Title, A., Wolfson, C.J., Zayer, I., and MDI Engineering Team: 1995, *Solar Phys.* **162**, 129.

Schwartz, R.A., Csillaghy, A., Tolbert, A.K., Hurford, G.J., Mc Tiernan, J., and Zarro, D.: 2002, *Solar Phys.* **210**, 165.

Siversky T. V., Zharkova V. V., 2009, A& A, **504**, 1057

Somov, B. V., Syrovatskii, S. I., Spektor, A. R.: 1981, *Solar Phys.* **73**, 145.

Su, Yang. and Holman, G.D. and Dennis, B.R. and Tolbert, A.K. and Schwartz, R.A.: 2009, *Astrophys. J.* **705**, 1584.

Sudol, J.J. and Harvey, J.W.: 2005, *Astrophys. J.* **635**, 647.

Syrovatskii, S.I. & Shmeleva, O.P., 1972, *Soviet Astron. J.*, **49**, 334.

Trottet, G., Rolli, E., Magun, A., Barat, C., Kuznetsov, A., Sunyaev, R., and Terekhov, O.: 2000, *Astron. Astroph.* **356**, 1067.

Wood, P. and Neukirch, T.: 2005, *Solar Phys.* **226**, 73.

Zharkova, V.V.: 2008, *Solar Phys.* **251**, 641.

Zharkova, V.V. and Kobylinskij, V.A.: 1989, *Soviet Astronomy Letters* **15**, N5, 366.

Zharkova, V.V. and Kobylinskij, V.A.: 1991, *Soviet Astronomy Letters* **17**, N1, 34.

Zharkova, V.V. and Kobylinskij, V.A..: 1993, *Solar Phys.* **143**, 259.

Zharkova V. V., Gordovskyy M., 2004, ApJ, 604, 884

Zharkova, V.V. and Gordovskyy, M., 2005a, *Astron. Astroph.* **432**, 1033.

Zharkova, V.V. and Gordovskyy M., 2005b, *M*NRAS, **356**, 1107.

Zharkova, V.V. and Gordovskyy, M.: 2006, *Astrophys. J.* **651**, 553.

Zharkova, V.V. and Zharkov, S.I.: 2007, *Astrophys. J.* **664**, 573.

Zharkova, V.V. & Agapitov, O.: 2009, *Journ. Plasma Phys.* **75**, N2, 159.

Zharkova V. V., Zharkov S. I., Ipson S. S., Benkhalil A. K., 2005, Journ.Geophys.Res., 110, 8104

Zharkova V. V., Kuznetsov A. A., Siversky T. V., 2010, A&A, 512, 845

Reply to the

Reviewer's Comments

We have addressed the concerns of the referee as follows:

C4-A4: The authors argue their case for "a pre-flare
event" on the basis of the temporal information in the light
curves only. However, I believe RHESSI imaging information is readily
available, so I would expect the authors to provide the spatial
association/information in the paper as well.

Answer to C4-A4.

There is some misunderstanding by the respected referee because in section 2.1 (from the last par.
on page 3, left column onwards) and Figure 2 (became Figure 3 in the revised version) in our paper
we described the images   obtained for the pre-flare event, in addition to the light curves.

The information from the light curves was used for initial decision about status of the small event.
Then, of course, it was confirmed by HXR images (see Fig 2 in the previous version or Fig. 3 in the
current one).

In the revised version we added 'The pre-flare event' to the caption of Figure 3 and clarified the
discussion of images for the preflare event, specifically the locations of the source B and its spatial
co-location with the HXR and H-alpha kernels in the main flare   (see Fig 6 and discussion about it).

Q8-A8: The referee is aware that the authors do not simulate HXR
spectrum in the paper. However, as the authors point out in the answer,
the electron beam parameters are derived from RHESSI HXR spectrum.
The beam parameters are dependent on the efficiency of HXR emission,
specifically thick-target HXR flux from the same electron flux in ionized
and neutral hydrogen will be different by some factor .
Therefore, the inferred electron spectrum will be dependent
whether the electrons emitting in the almost neutral
chromosphere or/and the fully ionized corona. I know at least
two works - Su et al, 2009, Kontar et al, 2002, who show that this
effect needs to be considered when RHESSI HXR spectrum is analyzed.
How does this effect the inferred parameters of the beam?

Answer to C8-A8.

 We agree that our answer to this comment was not clear in the previous reply. Now we try to clarify
this point.

With all due respect to the attempt to account for a partial ionization by Kontar et al., 2002 and Su et al, 2009 calculating HXR photon spectra for the simple Kramers cross-sections, we have to emphasize that their approach was still a very rude approximation for HXR emission by simple Kramers cross sections while Kontar et al. (2006), Kasparova et al, 2005 have specifically emphasized that for the interpretation of hXR emission in flares only relativistic cross-sections must be used. In the current paper we use the relativistic cross-sections by Ramaty and Bai where we corrected by misprints as described by Zharkova et al., 2010.

Also we need to emphasize that in the previous reply we have not clearly explained that our Fokker-Plank approach already considers a partial ionization in the collision frequency coefficient . The latter includes three terms: collisions with electrons, with protons and with neutrals (Zharkova and Kobylinsky, 1982; Siversky and Zharkova, 2009). This coefficient is made depth-dependent so that for each depth we used a temperature, density and ionization degree calculated for the relevant hydrodynamic model. As a matter of fact, we had about 70 depth points where the ionization degree deviated from 1. Also Dr. Holman asked V.Zharkova and she provided him with our HD models including this partial ionization as the last column of the model.

Therefore, our FP model contains all the effects of partial ionization, electric field and collisions plus the correct HXR bremsstrahlung cross-sections by Ramaty and Bai. We do not believe that any further improvements can be done for this rather comprehensive model.

However, we realized that the point about the partial ionization effect has not been clearly reflected in the paper text. In the revised version we have spelled explicitly these facts of our Fokker-PlanIck model (section 2.3.3., 3rd paragraph) and provided the reference to the papers by Kontar et al., 2002 and Su et al., 2009.

We hope the revised version will satisfy the respected referee comments and the paper becomes acceptable for a publication in MNRAS.

Sincerely Yours,

Valentina Zharkova,

on behalf of the co-authors